Respiratory Motion Compensation by Model-Based Catheter Tracking during EP Procedures

A. Brost[a,*], R. Liao[b], N. Strobel[c], J. Hornegger[a,d]

[a]*Pattern Recognition Lab, Department of Computer Science, Friedrich-Alexander-University Erlangen-Nuremberg, Erlangen, Germany*
[b]*Siemens Corporate Research, Imaging and Visualization, Princeton, New Jersey, USA*
[c]*Siemens AG, Healthcare Sector, Forchheim, Germany*
[d]*School in Advanced Optical Technologies (SAOT), Erlangen, Germany*

Abstract

In many cases, radio-frequency catheter ablation of the pulmonary veins attached to the left atrium still involves fluoroscopic image guidance. Two-dimensional X-ray navigation may also take advantage of overlay images derived from static pre-operative 3-D volumetric data to add anatomical details otherwise not visible under X-ray. Unfortunately, respiratory motion may impair the utility of static overlay images for catheter navigation. We developed a novel approach for image-based 3-D motion estimation and compensation as a solution to this problem. It is based on 3-D catheter tracking which, in turn, relies on 2-D/3-D registration. To this end, a bi-plane C-arm system is used to take X-ray images of a special circumferential mapping catheter from two directions. In the first step of the method, a 3-D model of the device is reconstructed. Three-dimensional respiratory motion at the site of ablation is then estimated by tracking the reconstructed catheter model in 3-D based on bi-plane fluoroscopy. Phantom data and clinical data were used to assess model-based catheter tracking. Our phantom experiments yielded an average 2-D tracking error of 1.4 mm and an average 3-D tracking error of 1.1 mm. Our evaluation of clinical data sets comprised 469 bi-plane fluoroscopy frames (938 monoplane fluoroscopy frames). We observed an average 2-D tracking error of 1.0 mm $\pm$ 0.4 mm and an average 3-D tracking error of 0.8 mm $\pm$ 0.5 mm. These results demonstrate that model-based motion-

---

[*]Corresponding author
   Email address: `Alexander.Brost@informatik.uni-erlangen.de` (A. Brost)

compensation based on 2-D/3-D registration is both feasible and accurate.

1. Introduction

Atrial fibrillation (AF) is one of the most common heart rhythm disorders and a leading cause of stroke. In the United States about two million people are affected by some form of AF. Radio-Frequency catheter ablation (RFCA) has become an accepted option for treating AF in today's electrophysiology (EP) labs, in particular, if drug treatment has become ineffective [1, 2].

Traditionally, RFCA of the pulmonary veins (PVs) has been carried out under fluoroscopy guidance. Unfortunately, X-ray projection images cannot distinguish soft tissue well. To address this issue, image integration combining pre-operative high-resolution 3-D atrial CT and/or MR volumes with the fluoroscopic images has been developed (fluoroscopic overlay image guidance). The potential advantage of this strategy is the fused display of the actual, real-time fluoroscopic images together with the highly detailed images from CT or MRI [3, 4, 5, 6]. In fact, state-of-the art C-arm systems [7, 8] facilitating 3-D tomographic reconstruction can also be used to obtain volumetric data sets of the heart [9, 10, 11, 12, 13, 14]. Two examples for bi-plane C-arm systems are shown in Figure 1. Since the 3-D data has been acquired on the same device that is also used for 2-D X-ray guidance, registration of the 3-D data set to the 2-D fluoroscopic projections is simplified. In addition to C-arm systems, cardiac mapping systems are available that provide catheter tracking without X-ray. Two common mapping systems are CARTO (Biosense Webster, Diamond Bar, CA, USA), and EnSite NavX (St. Jude Medical, St. Paul, MN, USA) [15, 16]. These mapping systems can be used to estimate a 3-D model of the heart. Model generation can be simplified by importing pre-operative CT, or MRI data sets [17, 18]. Unfortunately, mapping systems may add considerable cost to an EP procedure either because special catheters are needed, and/or because additional disposables enter the picture.

The most cost-effective therapy approach may be based on X-ray fluoroscopy involving overlay images derived from 3-D data sets. Unfortunately, current fluoroscopic overlay techniques are usually static. In other words, they do not account for respiratory and cardiac motion, i.e., they do not

2

(a) Artis **zee** Bi-plane with two large flat panel detectors (30 × 40 cm).

(b) Artis **zee** Bi-plane with two small flat panel detectors (20 × 20 cm).

Figure 1: Two bi-plane Artis **zee** C-arm systems with different detector configurations (Siemens AG, Forchheim, Germany). In general, the floor-mounted C-arm is denoted as *Plane A* and the ceiling-mounted C-arm as *Plane B*. These names are also used to denote with which C-arm an image or a sequence was acquired.

follow the heart while it beats and moves through the breathing cycle. Cardiac motion can be taken into account by synchronizing fluoroscopic images with the electrocardiogram (ECG). In this case, the residual motion is due to breathing. This motion needs to be compensated to achieve a dynamic fused visualization. While it has been widely recognized that motion compensation is crucial for fluoroscopic overlays, no image-based 3-D motion-compensation methods for EP applications have been proposed yet, at least to the knowledge of these authors. This may be due to the fact that there are few discernible features in typical EP fluoroscopic images. However, there is literature on dealing with motion for other applications. For example, motion compensated navigation for coronary intervention using magnetic tracking was suggested in [19], but it requires special catheters equipped with an electromagnetic sensor at increased cost. In the papers by [20] and [21] vertical motion in the imaging plane was compensated for liver embolization [22] and hepatic artery catheterization, respectively. The first paper [20] involved guidewire tracking, while the second method estimated motion by following the lung-diaphragm interface. In general, though, these methods are not sufficient for EP breathing motion compensation because the heart undergoes a three dimensional motion during respiration [23, 24]. As a consequence, motion estimation and subsequent compensation in 3-D is indispensable for accurate device navigation near or inside the left atrium (LA) throughout the breathing cycle as needed, e.g., for correct recording of ablation points.

Model-based 3-D motion estimation and compensation was proposed for coronary interventions and cardiac catheterization in [25, 26] and [27], respectively. A patient-specific motion model needs to be built beforehand in both methods, from either contrast-enhanced X-ray image sequences or MRI sequences. The underlying assumption here is one of reproducibility. Unfortunately, this may not always hold, because breathing patterns can vary in magnitude, period, and regularity [28].

This paper describes an image-based method to detect and compensate respiratory motion in 3-D using a bi-plane C-arm fluoroscopy device. A bi-plane X-ray system has two imaging planes commonly referred to as A-plane and B-plane, respectively. Motion compensation is achieved by tracking a circumferential, ring-shaped mapping catheter from two views. This (circumferential) mapping catheter is one of the most prominent structures visible in EP fluoroscopy scenes providing a good feature for robust tracking. During the isolation of the four pulmonary veins using radio-frequency catheter ablation, the mapping catheter is typically fixed at the ostium of the PV that is to be electrically isolated. By tracking the circumferential mapping catheter, we can obtain a motion estimate right at the ablation site, without the need of a pre-constructed motion model. Since we are using a bi-plane imaging system, the motion estimation takes place directly in 3-D and not in 2-D. Once an estimate of the 3-D motion is available, we can translate and rotate the 3-D data set accordingly and recompute a new fluoroscopic overlay using perspective rendering methods.

This paper is an extended version of previous work [29]. Compared to [29], substantially more experiments have been performed on both phantom and clinical data to provide a comprehensive validation of the proposed method. The paper is organized as follows: First, we describe how we generate a 3-D model of the circumferential mapping catheter from two views. Then we discuss model-based catheter tracking by 2-D/3-D image registration. Afterwards, we evaluate our method. Finally, we present our results, discuss them, and draw some conclusions.

2. Methods

2.1. 3-D Catheter Model Generation

The circumferential mapping catheter can be approximated as a circle in 3-D space when positioned at the ostium of the pulmonary vein. Our algorithm is based on the following two assumptions:
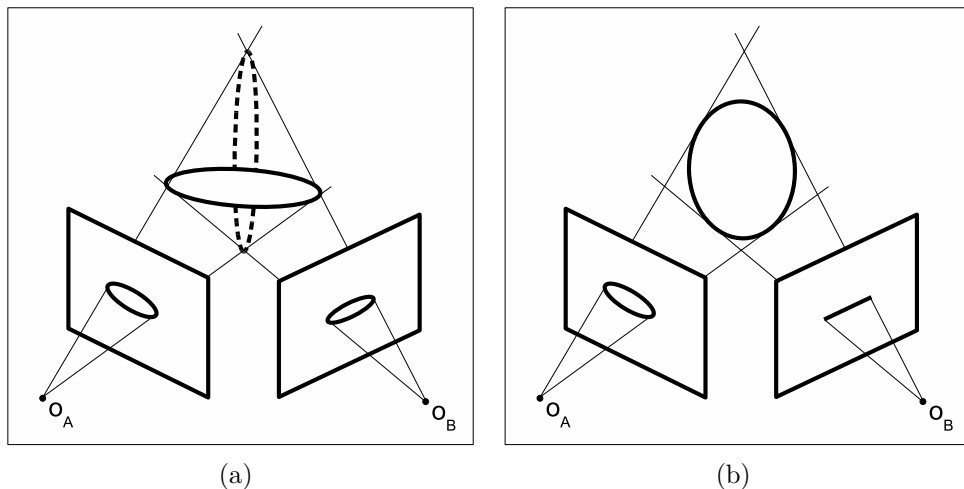
Figure 2: 3-D mapping catheter model initialization from two views. Figure 2(a): This *general case* shows two possible (dual) solutions when reconstructing a 3-D ellipse from bi-plane 2-D ellipses. The correct solution can be found by using prior knowledge, e.g., of the diameter of the circumferential mapping catheter. Figure 2(b): This *special case* reconstructs a 3-D ellipse from one 2-D ellipse in one X-ray view and a line in the other.

1. The circumferential mapping catheter - when fit to a pulmonary vein - can be approximated by a circle in 3-D space.
2. The projection of the circumferential mapping catheter into 2-D (X-ray) images can be modeled as a 2-D ellipse, with the special case of a 2-D line as an ellipse with one half axis being 0. The special case arises under some special C-arm viewing directions.

For the model generation, we differentiate between the regular case and the special case as shown in Figure 2. Note that we do not consider the case that the 3-D mapping catheter becomes a line in both X-ray projections as this is a very undesirable case in a clinical environment. Since C-arm devices can be rotated to change X-ray view directions, side views onto the 3-D object in both planes can be corrected by suitable C-arm positioning.

2.1.1. Ellipse Extraction in 2-D

For 3-D ellipse reconstruction, it is essential to know the 2-D ellipse parameters. So, the projection of the mapping catheter on the imaging plane is first extracted by manual clicking followed by fast marching in one frame of the fluoroscopy sequence, as explained in [30]. The 2-D ellipses are then

(a) Plane A   (b) Plane B
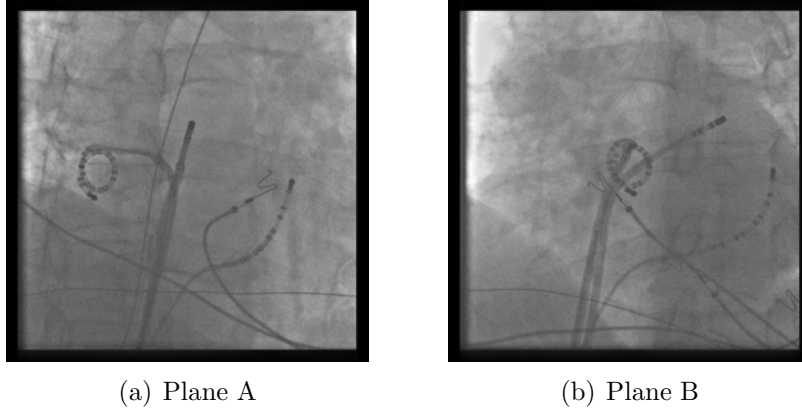
Figure 3: General case: the bi-plane C-arm system is set up such that the circular mapping catheter is projected as an ellipse in each view. Since a catheter has to be moved through the vessels of the body to reach its target, even a circular catheter has to have line-like characteristics including a catheter tip.

calculated such that all ellipse points satisfy the linear equation [31]

$$au_i^2 + bu_iv_i + cv_i^2 + du_i + ev_i + f = 0 \tag{1}$$

with the 2-D coordinates of the ellipse (u_i, v_i) and the coefficients of the ellipse $a, b, c, d, e, f \in \mathbb{R}$. Given a set of points $\mathbf{p}_i = (u_i, v_i)^T$ with $i = 1, \ldots, N$, these can be combined in a measurement matrix $\mathbf{M}$ [32]

$$\mathbf{M} = \begin{pmatrix} u_1^2 & u_1v_1 & v_1^2 & u_1 & v_1 & 1 \\ \vdots & \vdots & \vdots & \vdots & \vdots & \vdots \\ u_i^2 & u_iv_i & v_i^2 & u_i & v_i & 1 \\ \vdots & \vdots & \vdots & \vdots & \vdots & \vdots \\ u_N^2 & u_Nv_N & v_N^2 & u_N & v_N & 1 \end{pmatrix} \tag{2}$$

such that Eq. (1) is rewritten as

$$\mathbf{M} \cdot \mathbf{f} = 0 \tag{3}$$

with the (implicit) ellipse parameters $\mathbf{f} = (a, b, c, d, e, f)^T$. As the points may not necessarily lie exactly on the ellipse to be fitted, we are looking for the ellipse parameters $\hat{\mathbf{f}}$ that minimize

$$\hat{\mathbf{f}} = \arg\min_{\mathbf{f}} ||\mathbf{M}\mathbf{f}||_2^2 \tag{4}$$

6

(a) Plane A   (b) Plane B
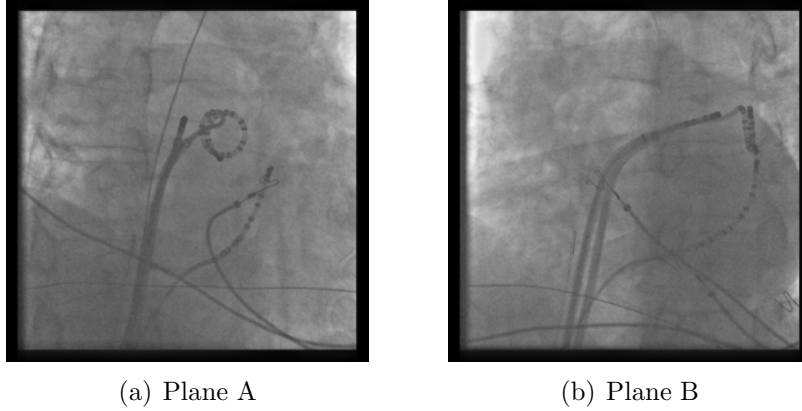
Figure 4: Special case: this viewing configuration can simplify bi-plane catheter navigation during ablation, where the circular mapping catheter often serves as a visual reference. In this view setup, the physician needs to verify that the ablation catheter is in the vicinity of its elliptical projection in one view and close to the line in the other.

subject to

$$||\mathbf{f}||_2 = 1. \tag{5}$$

Since the constraint $||\mathbf{f}||_2 = 1$ does not guarantee an elliptic solution, the method presented in [31] is used to assure the correct solution by enforcing the condition $b^2 - 4ac < 0$ [33, 34].

2.1.2. Ellipse Reconstruction in 3-D

For ellipse reconstruction from two views, we reformulate Eq. (1) as a matrix equation

$$\begin{pmatrix} u_i & v_i & 1 \end{pmatrix} \cdot \mathbf{C} \cdot \begin{pmatrix} u_i & v_i & 1 \end{pmatrix}^T = 0 \tag{6}$$

with the coefficients of the ellipse in matrix $\mathbf{C} \in \mathbb{R}^{3 \times 3}$ as

$$\mathbf{C} = \begin{pmatrix} a & \frac{1}{2}b & \frac{1}{2}d \\ \frac{1}{2}b & c & \frac{1}{2}e \\ \frac{1}{2}d & \frac{1}{2}e & f \end{pmatrix}. \tag{7}$$

As the ellipse points are projections of a circular object in 3-D space, we can write

$$\begin{pmatrix} x_i & y_i & z_i & 1 \end{pmatrix} \cdot \mathbf{P}^T \cdot \mathbf{C} \cdot \mathbf{P} \cdot \begin{pmatrix} x_i & y_i & z_i & 1 \end{pmatrix}^T = 0 \tag{8}$$

with the projection matrix $\mathbf{P} \in \mathbb{R}^{3 \times 4}$. The projection matrices were calculated using the method presented in [35, 36]. The matrix product $\mathbf{P}^T \cdot \mathbf{C} \cdot \mathbf{P}$

7

is replaced by $\mathbf{Q} \in \mathbb{R}^{4 \times 4}$, describing a cone in 3-D space with the optical center as origin and passing through the ellipse in the imaging plane. Given two projection images of an ellipse in 3-D on both A-plane view and B-plane view of a bi-plane system, respectively, we get two 3-D cones given by $\mathbf{Q}_A$ for imaging plane A and $\mathbf{Q}_B$ for imaging plane B. The reconstructed ellipse is then computed by calculating a λ such that [37]

$$\text{rank} \left(\mathbf{Q}_A + \lambda \cdot \mathbf{Q}_B \right) = 2. \tag{9}$$

Two possible solutions for the reconstructed ellipse in 3-D space can be found (Figure 2). In our application, we utilize our prior knowledge about the pseudo-circular shape of the circumferential mapping catheter and select the result that is more circular, because the circumferential mapping catheter inserted into a pulmonary vein resembles a circle more closely than an ellipse in normal human anatomy. The circularity is determined by:

$$\kappa = |\phi - \psi| \tag{10}$$

with the axes ϕ and ψ of an ellipse. To obtain the more circular solution, the ellipse with the smaller value for κ is used.

For the special case where the circumferential mapping catheter is projected close to being a line in one view, the method in [37] is not stable, as this method requires for $\mathbf{Q}_A$ and $\mathbf{Q}_B$ to be of rank three. Unfortunately, if a line is described by the matrix $\mathbf{C}$, this matrix is already of rank two. Thus the multiplication of $\mathbf{P}^T \cdot \mathbf{C} \cdot \mathbf{P}$ leads to a matrix of rank two. This special case is detected by considering the rank of the measurement matrix containing the first and second order point coordinates [31]

$$\mathbf{M}' = \sum_i \begin{pmatrix} u_i^2 & u_i v_i & u_i \\ u_i v_i & v_i^2 & v_i \\ u_i & v_i & 1 \end{pmatrix}. \tag{11}$$

A rank deficiency indicates a linear dependency and therefore an ellipse that collapsed to a line. In this case, we propose to reconstruct the 3-D mapping catheter model by the following procedures. First, a line is fitted to the line-like projection of the mapping catheter. It is calculated as the principal axis of the points obtained by fast marching. Two arbitrary but distinct points $\mathbf{q}_1$ and $\mathbf{q}_2$ are then randomly selected on the fitted line and are connected to the optical center. The projection plane in which both the X-ray source and the

8

fitted line lies is then determined by the two rays $\mathbf{q}_{1,o}$ and $\mathbf{q}_{2,o}$. In the second and final step, the 3-D mapping catheter model is obtained by intersecting this plane with the elliptical cone defined by the ellipse from the second view. We propose the following method to calculate the analytical formulation of the conic section that intersects a plane $\widetilde{\mathbf{n}} = (x_n, y_n, z_n, d_n)^T$ with an elliptical cone $\mathbf{Q}$. The key idea is to transform the original coordinates, taken with respect to the iso-center of the C-arm system, to new coordinates, in which the transformed x-y-plane coincides with the cutting plane $\widetilde{\mathbf{n}}$. The transformation is given as

$$\mathbf{S} = \begin{pmatrix} \mathbf{u} & \mathbf{v} & \mathbf{n} & 0 \\ 0 & 0 & d_n & 1 \end{pmatrix} \tag{12}$$

where $\mathbf{n} = (x_n, y_n, z_n)^T$ is normalized to unit length, and $\mathbf{u}$ and $\mathbf{v}$ can be any pair of unit length vectors lying in the cutting plane that are orthogonal to each other. $\mathbf{S}$ therefore presents a standard rigid-body transformation matrix after which the conic section $\mathbf{w}' = \mathbf{S}\mathbf{w}$ lies in the transformed x-y-plane with $z' = 0$. In addition, since

$$(\mathbf{w}')^T \mathbf{U} \mathbf{w}' = 0 \qquad \text{with} \qquad \mathbf{U} = (\mathbf{S}^{-1})^T \mathbf{Q} \mathbf{S}^{-1} \tag{13}$$

and considering $z' = 0$, the parameters of the analytical formulation of the conic section can be obtained straightforwardly from the matrix $\mathbf{U}$ by $\hat{a} = u_{1,1}$, $\hat{b} = 2u_{1,2}$, $\hat{c} = u_{2,2}$, $\hat{d} = 2u_{1,4}$, $\hat{e} = 2u_{2,4}$, $\hat{f} = u_{4,4}$ where $u_{i,j}$ represents the element of the i-th row and j-th column of matrix $\mathbf{U}$. The model points in the transformed coordinate system are given as $\mathbf{w}'_i$ (in homogeneous coordinates), $i = 1, \ldots, L$, with the number of model points L, and are calculated using the estimated ellipse parameters $\hat{a}, \hat{b}, \hat{c}, \hat{d}, \hat{e}, \hat{f}$ as explained above. The 3-D points for the model of the circumferential mapping catheter in the C-arm isocenter coordinate system, $\mathbf{w}_i$ (in homogeneous coordinates), are then calculated by $\mathbf{w}_i = \mathbf{S}^{-1} \mathbf{w}'_i$.

2.2. Model-Based Catheter Tracking

After the 3-D model of the circumferential mapping catheter has been generated from the first frame of the fluoroscopic sequence, it is tracked in 3-D throughout the remainder of the bi-plane sequence by performing 2-D/3-D registration on pre-processed X-ray images. The use of a bi-plane system facilitates the estimation of a 3-D motion, but techniques are conceivable where motion-compensation could be performed from one direction as well.

But to assess their merits, it is essential to establish benchmark results using bi-plane imaging. The term *images* refers to the corresponding frames of viewing plane A and of viewing plane B, respectively. The images are pre-processed to improve the quality of the registration.

In the first pre-processing step, the region of interest (ROI) for tracking is cut to 400×400 pixels (on the 1024×1024 image) around the center of the tracked mapping catheter in the previous frame. This speeds up the algorithm, and it also minimizes the influence of peripheral structures that could interfere with catheter tracking. Histogram equalization on the ROI is applied next to increase image contrast. In addition, a vessel enhancement filter as proposed in [38] is used to enhance line-like structures such as the circumferential mapping catheter. The feature image is then binarized using Otsu's algorithm [39]. This facilitates segmentation of the mapping catheter. Finally, a distance map is calculated from the binarized image [40], where the distance map encodes the distance from a point to its closest feature point, that is the nonzero point representing the extracted mapping catheter in our binarized feature image. The distance map is further denoted as $\mathbf{I}_{\mathrm{DT}}$ with $\mathbf{I}_{\mathrm{DT}}(\mathbf{p})$ accessing pixel $\mathbf{p}$ of the distance map. The resulting value is the distance of pixel $\mathbf{p}$ to the closest feature point. The distance transform offers an important advantage. It provides a denoised representation of the fluoroscopic image with a pronounced minimum around the 2-D shape of the circumferential mapping catheter. As a consequence, we can still reach a good registration, even if we have a small 3-D model error, or if we start from a position that is somewhat distant from the mapping catheter to be tracked.

Model-based catheter tracking in 3-D is achieved by performing 2-D/3-D registration. To this end, the reconstructed 3-D catheter model is rotated by $\mathbf{R}$ and translated by $\mathbf{T}$ in 3-D first. Then it is projected onto the two imaging planes of the bi-plane C-arm system. The average distance between the projected points and the closest feature point (i.e. the circumferential mapping catheter) in fluoroscopic images is efficiently calculated using the distance map introduced above. A suitable rotation and translation is found by optimizing

$$\hat{\mathbf{R}}, \hat{\mathbf{T}} = \arg\min_{\mathbf{R},\mathbf{T}} \sum_i \mathbf{I}_{\mathrm{DT}}(\mathbf{P}_A \cdot \mathbf{T} \cdot \mathbf{R} \cdot \mathbf{w}_i) + \sum_i \mathbf{I}_{\mathrm{DT}}(\mathbf{P}_B \cdot \mathbf{T} \cdot \mathbf{R} \cdot \mathbf{w}_i). \quad (14)$$

The parameters used for optimizing are three rotation angles around the main axes in 3-D, combined in $\mathbf{R}$, as well as a three-dimensional translation,
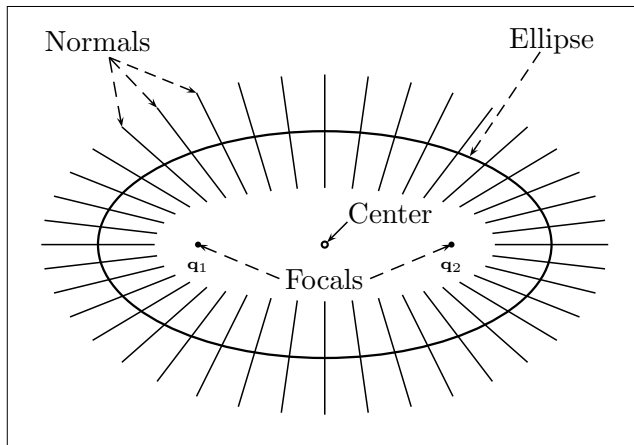
Figure 5: Two-dimensional ellipse with center (circle), focal points (dots), $\mathbf{q}_1$ and $\mathbf{q}_2$, and normals $\mathbf{n(p)}$.

represented in $\mathbf{T}$. As optimization strategy, a nearest neighbor search [41] is used, i.e., the position of the local optimum on a large scale is taken as starting point for the optimization on a smaller scale. However, due to the fact that the shape of mapping catheters may not always be exactly elliptical, a simple elliptical 3-D model may not fit perfectly. To still obtain robust tracking, the distance of a forward projected 3-D point to the closest feature point is calculated as the smallest distance among all the points along the normal direction within five pixels from the projected point. An illustration of the normals to an ellipse is given in Figure 5. The normal $\mathbf{n}$ to a point $\mathbf{p}$ on the ellipse is calculated by [42]

$$\mathbf{n(p)} = \frac{1}{2} \left[(\mathbf{q}_1 - \mathbf{p}) + (\mathbf{q}_2 - \mathbf{p}) \right] \tag{15}$$

with the focal points $\mathbf{q}_1$ and $\mathbf{q}_2$ of the ellipse. A best neighbor optimizer is used to iteratively optimize the translational and rotational parameters. Registration is performed in two steps. In the first step, only the translation is considered, whereas in the second step a fully six-dimensional optimization is performed. Two-step registration is implemented to increase performance by lowering the number of iterations required for optimization. Depending on the actual frame rate used for image acquisition, the inter-image movement may be larger for lower frame rates, e.g., 1 frame-per-second for ECG-triggered fluoroscopic acquisition. The first registration step covering only

11
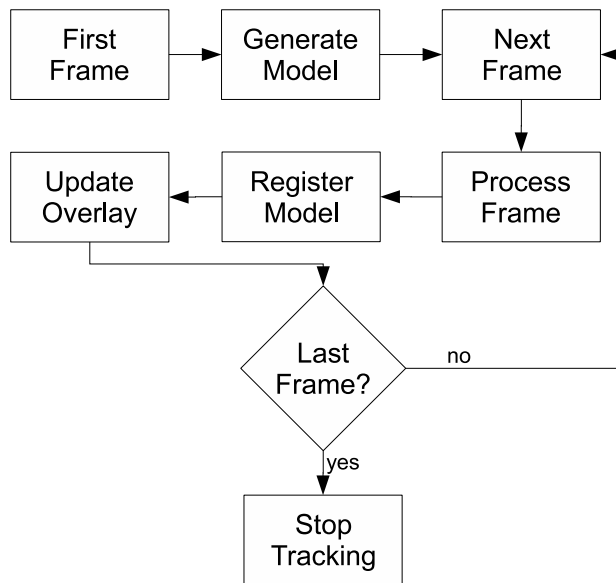
Figure 6: Flow diagram of our motion compensation approach. The objective is to obtain a dynamic fluoroscopic overlay image for improved catheter navigation.

the translational parameters helps to increase the search range without reducing the computational performance. After an initial best fit is found, the translational and rotational parameters are optimized on a smaller scale. Our tracking algorithm is briefly summarized in Figure 6. An overview of the image preprocessing and registration steps is presented in Figure 7.

3. Experiments

3.1. Model Generation

Our goal is to estimate motion by registering a 3-D model of a circular mapping catheter to two associated 2-D projections taken simultaneously under two different viewing angles using bi-plane X-ray imaging systems as displayed in Figure 1. Rigid three-dimensional motion can then be estimated, for example, by successively estimating the 3-D position and orientation of the ellipse after successful registration. This approach depends on an accurate estimate for a model of the circumferential catheter used. In what follows, we evaluate the accuracy of our catheter model generation step. We start with simulations before we turn to experiments involving actual X-ray projections. In our simulations, five circles in 3-D space were set up,
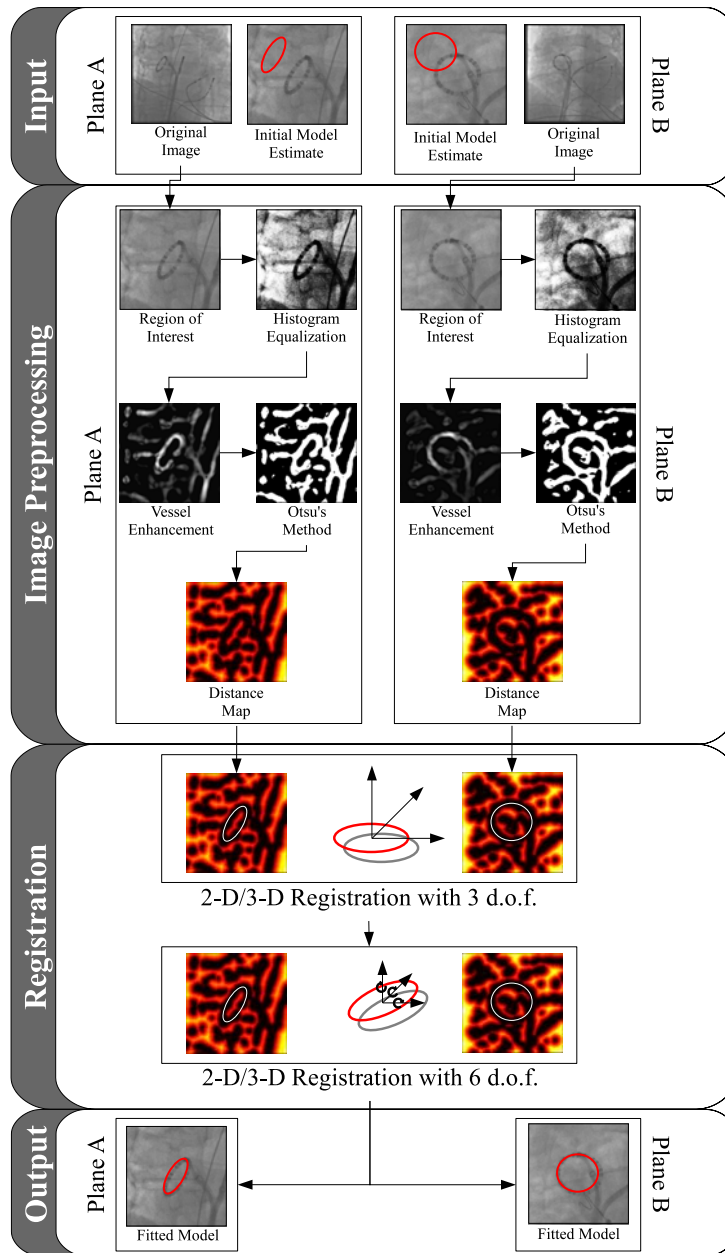
Figure 7: Detailed illustration of the image preprocessing and the registration step.
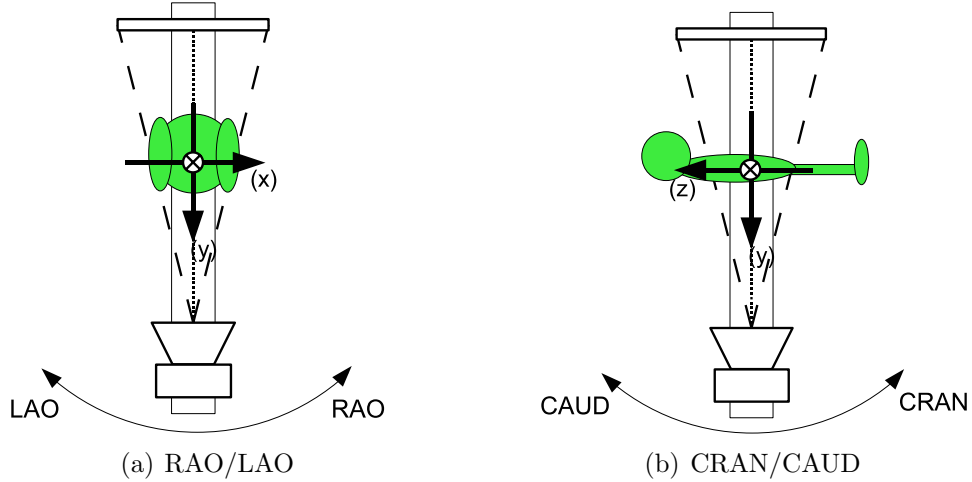
Figure 8: Basic geometry of a C-arm X-ray imaging system. (a) illustrates the rotation of the C-arm related to a patient's right/left side, right anterior oblique (RAO/LAO), viewed from a patient's feet side. (b) illustrates the rotation towards a patient's cranial (head) or caudal (feet) (CRAN/CAUD) direction, viewed from a patient's right side. The illustration is referring to [35].

each with a different position, orientation and diameter. These five 3-D circles were forward projected onto 2-D imaging planes for a set of C-arm projection angles. In the next step, these 3-D circles were reconstructed by triangulation. C-arm positions are defined by two angles, the first angle denotes the rotation of the C-arm related to a patient's right/left side, right anterior oblique (RAO/LAO). The second angle denotes the rotation towards a patient's cranial (head) or caudal (feet) (CRAN/CAUD) direction. See Fig. 8 for an illustration. The reconstruction was done for the C-arm position angles (RAO/LAO) $\in [-90°, -60°, -30°, \ldots, 60°, 90°]$ with (CRAN/CAUD) $= 0$. The latter was chosen to be 0 as this is the usual setup for electrophysiology procedures. In other words, the space of all used C-arm detector positions was subsampled in steps of 30°, given a minimum angular difference of 30° and a maximum difference of 150° between two C-arm views used for 3-D ellipse reconstruction by triangulation. The cases considering an angular difference of 0° and 180°, respectively, were omitted during the simulation. Not all of these viewing angles are useful in a clinical environment but the results give a systematic evaluation of the accuracy of our reconstruction method. The overall error is calculated as the average

14

distance between points on the original 3-D circle and their nearest-neighbor counterparts on the reconstructed circle. Four cases were evaluated. In the first case, we simply reconstructed a 3-D circle from the projection images not adding any noise to find out how the reconstruction method works in an idealized scenario. In the other experiments, we added Gaussian noise with zero mean and a standard deviation of up to 2.0 mm to the 2-D points before reconstructing the 3-D object. This is to simulate the potential noise in the mapping catheter point localization step. For a typical EP fluoroscopy image with size of 1024×1024, 2.0 mm equals to ≈ 12 pixels on the imaging plane. We also added a translational error in one imaging plane of up to 2.0 mm, simulating the potential relative shift in the mapping catheters detected in the two imaging planes. The relative shift between plane A and plane B images can be either due to the fact that a mapping catheter is not a thin line but of certain width, or because there is inaccuracy in the geometrical calibration between plane A and plane B.Finally, we simulated both Gaussian noise and translational error. The results are summarized in Figure 9. The errors listed in the table were calculated by averaging individual errors over the five circles reconstructed from the bi-plane C-arm angulations considered. The general case refers to the situation where an ellipse was visible in both imaging planes. The special case implies that there was one ellipse in one view, while it collapsed to a line in the other view. The projection matrices for the simulation were computed as described in [35, 36].

Our simulation results show that 3-D reconstruction is very accurate under ideal conditions, but the error increases noticeably when there is noise, see Figure 9. Put differently, 3-D ellipse reconstruction from two views is very sensitive to noise in the 2-D points of the detected ellipse, especially when a translational error is present. To deal with this problem, high-precision ellipse detection and geometrical calibration between plane A and plane B is required for initial model generation in the general case.

To further validate our approach, we acquired bi-plane fluoroscopic images of a static catheter from different viewing directions and compared the 3-D reconstruction results to a 3-D data set reconstructed using C-arm CT on the same system. C-arm CT involved X-ray data acquisition on an AXIOM Artis dBA bi-plane system (Siemens AG, Forchheim, Germany). First, the A-plane performed a partial circle scan around the experimental setup. Then, a 3-D data set was reconstructed using a *syngo* X-Workplace running *syngo* DynaCT (both Siemens AG, Forchheim, Germany). The system was calibrated using the method presented in [43]. The 3-D coordinates of the cir-
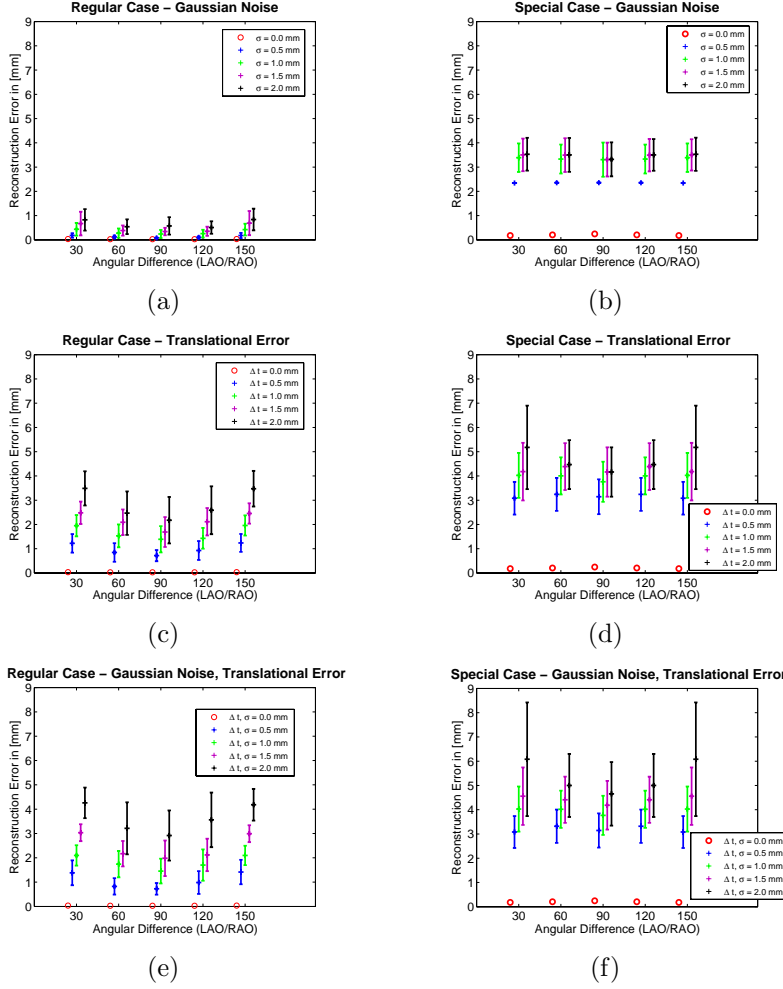
Figure 9: Simulation results for 3-D catheter model generation from bi-plane views. The error is given with its standard deviation. (a) Reconstruction from two 2-D ellipses. The 2-D points were disturbed by Gaussian noise with zero mean and an increasing standard deviation, 0.5 mm to 2.0 mm. According to the pixel spacing considered for the simulation, a 2-D noise of 1 mm equals to ≈ 6 pixels on the imaging plane. The errors were calculated by averaging individual errors over the five circles reconstructed from the angulation considered. (b) Reconstruction from one ellipse and one line, with Gaussian noise. (c) Reconstruction from two ellipses with a translational error. (d) Reconstruction from one ellipse and one line, with translational error. (e) Reconstruction from two ellipses with Gaussian noise and translational error. (f) Reconstruction from one ellipse and one with Gaussian noise and translational error.
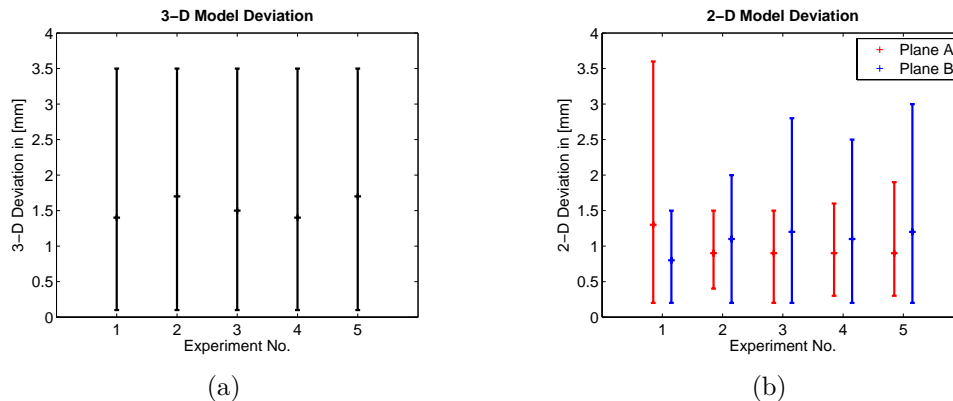
Figure 10: Experimental results for 3-D model generation by triangulation from two views. Five experiments were carried out to evaluate the accuracy. The experimental setup, i.e., the position of the C-Arms and the position and orientation of the mapping catheter, was chosen to be as close as possible to a clinical setup. (a) The 3-D deviation represents the average distance between the reconstructed catheter to a manually outlined catheter in a 3-D data set. The minimum and maximum deviation is also presented. On average over all five experiments a model generation error of 1.5 mm was achieved. (b) The 2-D deviation represents the mean deviation of the projected 3-D model into each imaging plane from the original 2-D segmentation. The minimum and maximum deviation is also presented. An average deviation over all five experiments of 1.0 mm for plane A and 1.1 mm for plane B was achieved.

cumferential mapping catheter were manually obtained from the 3-D volume and compared to the 3-D reconstruction results obtained from biplane views. To mimic a clinical setup, we varied only the primary angle (LAO/RAO), as it would be during an EP procedure. The secondary angle (CRAN/CAU) was kept constant. The experimental results for catheter model generation are given in Figure 10. The 3-D model deviation is mostly influenced by the position and the size of the reconstructed catheter model. The 2-D model deviation is moreover influenced by the shape of the catheter in the 2-D fluoroscopic images. If the catheter can not be approximated well by an ellipse, a larger model deviation occurs.

3.2. Model-Based Catheter Tracking

After a 3-D model of the circumferential mapping catheter has been set up from the first frame of the bi-plane fluoroscopic sequence, the position of this 3-D model is continuously adjusted by performing 2-D/3-D registration.

We evaluated our algorithm on five bi-plane fluoroscopy sequences that
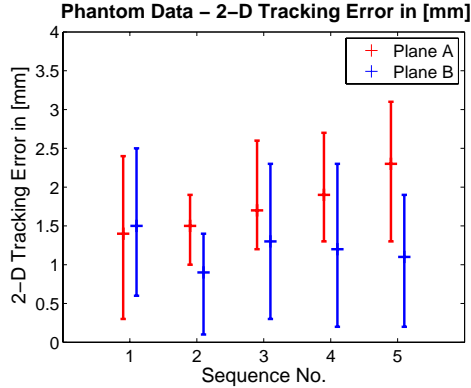
Figure 11: Average 2-D tracking error for the sequences used involving a moving heart phantom. The mean error and its minimum and maximum are shown. The tracking error for plane A averaged over all sequences yielded an average error of 1.6 mm, a total minimum of 0.3 mm and a total maximum of 3.1 mm. The tracking error for plane B yielded an average of 1.2 mm, a total minimum of 0.6 mm and a total maximum of 2.5 mm, respectively. The total number of frames was 173.

were acquired using a moving heart phantom to which the mapping catheter was fixed, mimicking the situation when the catheter is placed at the ostium of one of the pulmonary veins. We also calculated the tracking error throughout nine different clinical fluoroscopic sequences that were acquired during EP procedures on an AXIOM Artis dBA C-arm system (Siemens AG, Forchheim, Germany). The system was calibrated using the method presented in [43]. We focused on scenes recorded during ablation for atrial fibrillation that show one circumferential mapping catheter and one ablation catheter. The presence of other structures should not decrease the accuracy of our method, because we use a unique elliptical structure for registration.

To study the tracking error in 2-D, we forward projected the 3-D catheter model, computed from the first frame, into both planes of the bi-plane imaging system after 2-D/3-D registration. The first frame is used to set up a 3-D model of the circumferential ablation catheter. As no 2-D/3-D registration is performed in this particular frame, it is only affected by a model error. The model error expresses how well the 3-D model fits to its associated 2-D projections it was generated from. Starting with the second frame, we calculated the average 2-D distance of the forward projected 3-D catheter model to a manually segmented mapping catheter. An example for a bi-plane frame is shown in Figure 13 for clinical data. The manual catheter segmentation in
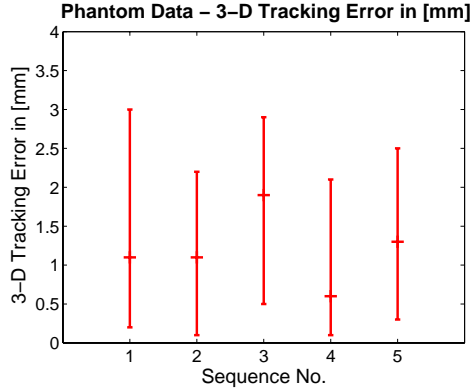
Figure 12: The mean 3-D tracking error as well as the minimum and maximum tracking error in mm for each sequence of the moving heart phantom, over 173 bi-plane fluoroscopy frames. An average error of 1.1 mm over all five sequences was achieved with a total minimum error of 0.1 mm and a total maximum error of 3.0 mm.
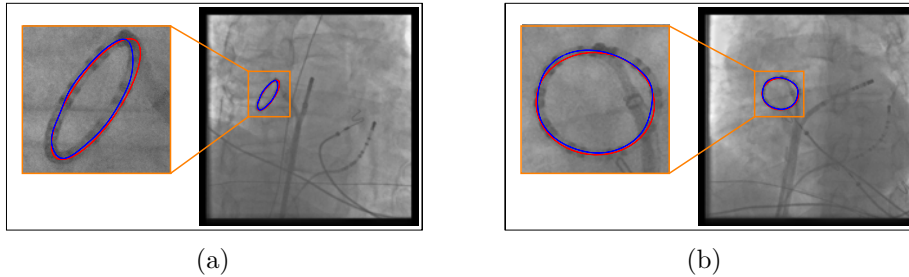
Figure 13: (a) Tracked ellipse (red) in plane A. It has an average distance to the manual segmentation (blue) of 1.0 mm (model error 0.5 mm). (b) In this particular frame, the tracking error (0.6 mm) is completely due to the model error (0.6 mm).

each fluoroscopic frame was supervised by a cardiologist, and we consider it our reference result. The 2-D distances between the forward projected 3-D model and the manually segmented reference in each fluoroscopic frame of a sequence were averaged over all frames to arrive at an overall 2-D tracking error for each sequence. It is expressed in terms of mean and standard deviation.

To evaluate the 3-D accuracy of our motion estimation approach based on model-based catheter tracking, we selected the tip of the circumferential mapping catheter as a reference point. The tip of a circular catheter can, e.g., be seen nicely in Figure 3. During EP ablations, the main region of interest
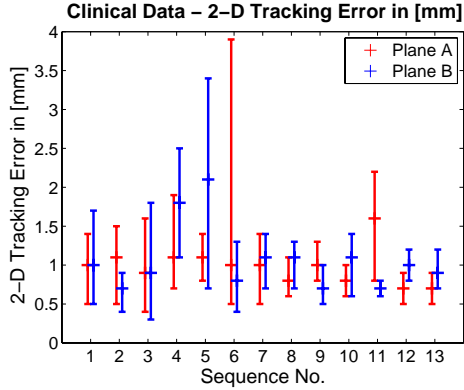
Figure 14: Average 2-D tracking error as well as the minimum and maximum tracking errors for the clinical sequences used. For plane A, an average error over all sequences of 1.0 mm was achieved with a total minimum error of 0.4 mm and a total maximum error of 3.9 mm. The maximum error was due to the overlap with contrast agent which in one frame occluded For plane B, an average error of 1.0 mm, a total minimum error of 0.3 mm and a total maximum error of 3.4 mm was achieved, respectively. The total number of frames was 469 for each imaging plane.

in the overlay that requires motion compensation is the pulmonary vein being ablated. To obtain good tissue contact, the mapping catheter is typically pushed against the wall of the left atrium preventing it moving relative to it. This is why the tip of the mapping catheter is a good reference point for tracking error quantification. The tip was manually localized throughout all sequences by triangulating its 3-D position from bi-plane frames to get a reference first. In the next step, we applied the motion estimated by catheter tracking to the catheter tip to move it from one 3-D position to the next. Finally, we compared the 3-D position reached by applying the estimated motion to the actual 3-D reference point obtained by triangulation, as described in [36, 35]. In the end, the error was calculated as the Euclidean distance in 3-D space.

The 2-D and 3-D tracking error for the circular catheter attached to the moving heart phantom are listed in Figure 11 and Figure 12, respectively. In Figure 11, the 2-D error was computed for each of the two imaging planes, i.e., for Plane A as well as for Plane B. The average over the mean tracking errors obtained for the sequences recorded with the moving heart phantom was 1.6 mm ± 0.6 mm for plane A and 1.2 mm ± 0.5 mm for plane B. The A-plane model errors were between 0.4 mm and 1.3 mm, while the B-plane

20
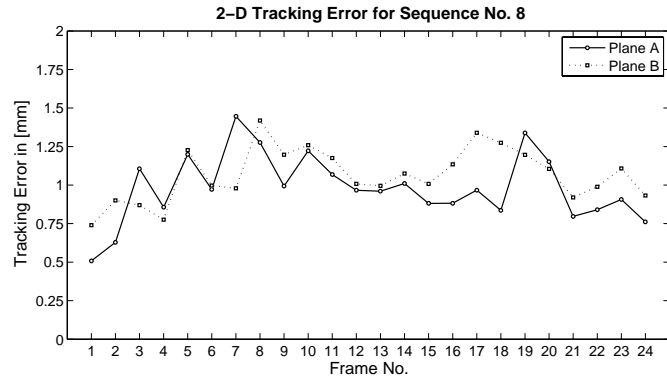
(a)
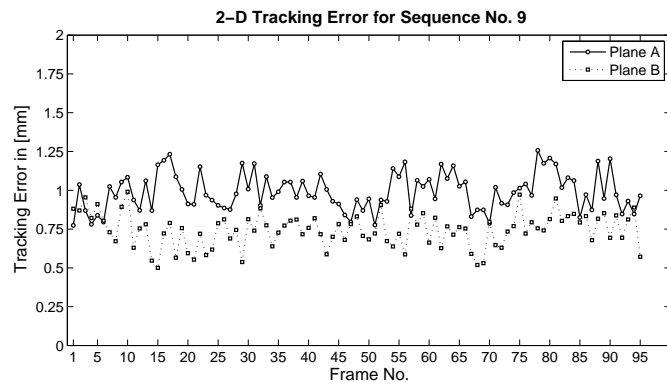
(b)
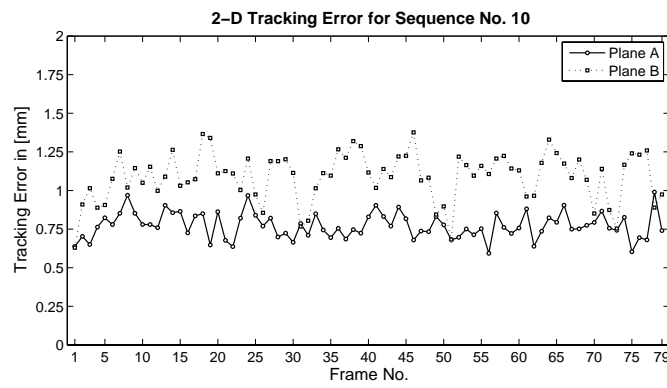
(c)

Figure 15: Two-dimensional tracking error in mm for three different sequences frame by frame.

21
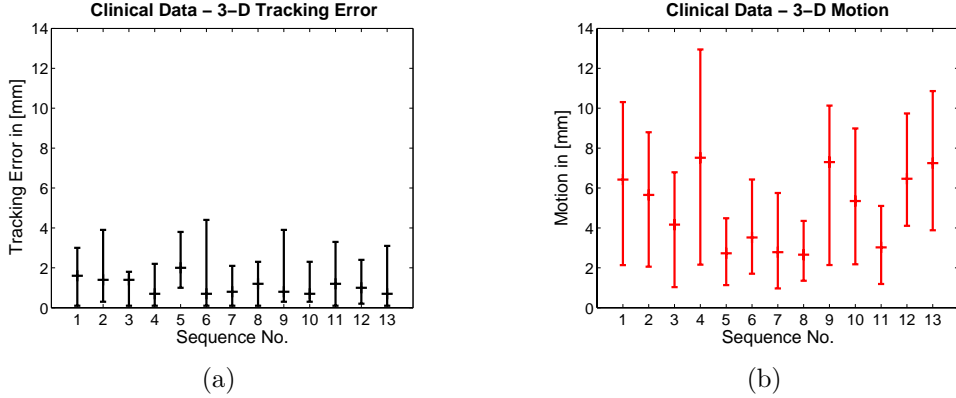
Figure 16: Tracking error and motion for the tested clinical sequences. (a) The mean 3-D tracking error in mm for each sequence, with the minimum and maximum error. (b) The mean 3-D motion in mm for each sequence, with the minimum and maximum motion. The 3-D motion is the length of the motion vector.

model errors ranged between 0.8 mm to 1.2 mm.

Both A-plane and B-plane tracking results for each of the nine clinical sequences are summarized in Figure 14. The tracking in sequence no. 5 suffers from the fact, that in imaging plane B the mapping catheter is not a closed ellipse. The ground truth segmentation outlines only the catheter. Hence, although the tracking is accurate, as it can be seen from the 3-D tracking error presented in Figure 16, the deviation from the gold-standard segmentation is biased. In sequence no. 6, the mapping catheter is in one frame hidden by barium swallowed to emphasize the esophagus. This also leads a higher 3-D tracking error, but right after the occlusion, the catheter is successfully tracked. The average over the mean tracking errors obtained for the clinical sequences was 1.0 mm ± 0.4 mm for plane A and 1.0 mm ± 0.4 mm for plane B. An example for one frame of one sequence is given in Figs. 13. The A-plane model errors were between 0.4 mm and 0.8 mm, while the B-plane model errors ranged between 0.3 mm to 1.1 mm. A detailed frame-by-frame 2-D tracking error for three different sequences is given in Figure 15. As the tracking errors range with a certain deviation, a drift in the tracking cannot be recognized. Looking at the frame-by-frame tracking error, as shown in Figure 15, we can see that our tracking algorithm does not suffer from error propagation. This is due to the tracking by registration approach. Every new frame is processed without incorporating too much knowledge of the previous frame or previous movement. Only the catheter

22
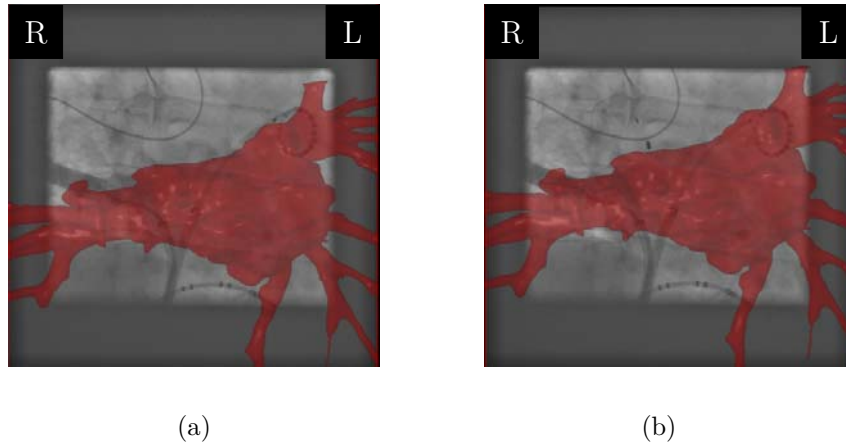
Figure 17: (a) Frame of a non-motion compensated sequence with fluoroscopic overlay. (b) The same sequence with motion compensation. Note how well both mapping catheter and contrast agent are matched to the morphology of the LA.

position within the previous frames is used as center of the region of interest, while the 3-D mapping catheter model stays unchanged during the tracking of the complete sequence. Therefore, even if there is a slight error in tracking the previous frame, tracking of the subsequent frame can still be highly accurate as long as the starting position lies within the capture range of the registration algorithm. In comparison, tracking algorithms that either require online updating of the appearance model, e.g., template-based method, or methods that rely heavily on temporal correlation among consecutive frames, e.g., motion model-based method, may suffer from drifting effect. The mean 2-D tracking error over 469 bi-plane fluoroscopy frames (938 monoplane fluoroscopy frames) was 1.0 mm $\pm$ 0.4 mm.

4. Discussion and Conclusions

We developed a method for 3-D motion estimation for radio-frequency catheter ablation of atrial fibrillation. A bi-plane X-ray C-arm system is used to simultaneously image a circumferential mapping catheter from two directions. Catheter tracking is based on 2-D/3-D registration principles. To this end, a 3-D catheter model is computed from the first frame of a fluoroscopic sequence. Simulations have shown that the model generation is accurate and less sensitive to Gaussian noise than to translational errors. Translational errors can be avoided by proper system calibration, and approx-

imating the circumferential catheter by an ellipse close to the center of its cross-section. Our experiments showed an average Euclidean distance from a real catheter to its reconstructed model of about 1.5 mm. The reconstructed catheter model is then forward projected onto both imaging planes. There, it is registered by minimizing an error based on a distance map derived from the fluoroscopic images. Note that the use of a distance map-based 2-D/3-D registration algorithm facilitates robust tracking even if the 3-D model does not exactly match. As long as the 3-D model is registered to its associated 2-D projections in successive frames consistently, an accurate motion estimate can be obtained. In our experiment involving a moving-heart phantom, we found a mean 2-D tracking error of 1.4 mm $\pm$ 0.6 mm with an average model error of 1.0 mm. When evaluating clinical EP fluoroscopic sequences, we determined an average 2-D tracking error of 1.0 mm in the presence of an average model error of 0.4 mm. The real tracking accuracy is therefore smaller than 1 mm. The results presented show a slightly higher error for data acquired with the moving-heart phantom. We attribute this result to the fact that our method was optimized for clinical data sets involving different circumferential mapping catheters than the one available for our experiments. Although unfortunate at first sight, this situation actually provided us with an opportunity to show that our method is robust by running it as is on the experimental data as well, i.e., without re-optimizing the algorithm parameters.

The proposed method offers several advantages. First, it is workflow-friendly and does not require any fiducial markers or additional contrast agent. Second, 3-D motion is estimated directly at the site of ablation. There is no ambiguity coming from the inference of the real motion from surrogate motion estimates. Third, motion estimation and compensation is performed in one step. Therefore we do not need a motion model as part of the estimation algorithm. Fourth, our method does not place any restrictions on the 3-D data set that can be used. In other words, the fluoro overlay could be rendered from 3-D data sets acquired using MRI, CT, or C-arm CT such as *syngo* DynaCT Cardiac (Siemens AG, Forchheim, Germany). Since the motion of the LA can be approximated by a rigid-body transform [44], it is possible to apply the motion estimate obtained by 3-D catheter tracking to the static fluoroscopic overlay. This way, we can obtain an animated version of our initial overlay that moves in sync with the real anatomy. Figure 17(a) represents the conventional overlay technique without motion compensation, while Figure 17(b) shows an animated fluoroscopic overlay with motion com-

pensation. With motion compensation, dynamic overlay and circumferential mapping catheter, fixed at the PV ostium, stay aligned. In addition, the contrast enhanced upper pulmonary vein, shown on the left side of the fluoroscopy image in Figure 17(b), matches well to the corresponding vein of the volumetric data. As far as accuracy is concerned, our 3-D motion error analysis yielded an average 3-D tracking error of 0.8 mm over 13 clinical data sets. This is superior to existing methods that provide an accuracy of 2.0 mm [45, 46]. It also appears acceptable in clinical practice as our error is below 2 mm [47]. Other work for motion correction in coronary interventions [25] yielded a displacement error of about 4.4 pixels to 7.1 pixels. Since the pixel spacing and image size was not stated in the paper, it is not clear what the displacement error was in millimeters. Respiratory motion compensation for MRI-guided interventions such as cardiac catheterisation [27] reports an error of 2 mm to 4 mm and for coronary MR angiography [48] of less than 2 mm. The work in [25, 27, 48] facilitates motion compensation by patient-specific motion model generation from pre-operative data sets. Our presented method does not need the generation of a specific motion model and requires less prior information.

Our method assumes that the circumferential mapping catheter remains anchored at the pulmonary vein being ablated. Our clinical data suggests that the circumferential mapping catheter moves very little with respect to the PV ostia as we assumed as it is used to measure the electrical signals at the specific locations of the pulmonary ostia to keep the catheter in close tissue contact for good signal measurements. Nevertheless,further validation and quantification is needed before a more precise statement can be made. This is part of ongoing research.

The current implementation of this algorithm achieves a frame rate of 3 frames-per-second using a single threaded CPU implementation. The image preprocessing took 70.6 ms and the registration 265.8 ms. At clinical sites where this frame rate is used for EP procedures to keep X-ray dose low, real-time catheter tracking can be achieved already. In other cases, either a faster implementation is needed, or better hardware is required. In sum, these results demonstrate that model-based motion-compensation by 2-D/3-D registration is both feasible and accurate. The proposed method is of general form and can be straightforwardly extended to other applications where bi-plane X-ray imaging is used to guide the interventions and a 3-D model for the navigation/intervention devices can be obtained, e.g. the linear catheter used in hepatic artery catheterization shown in [21]. Model-based 2-

D/3-D registration with the usage of a distance map then can be applied for robust motion estimation. For applications where the device to be tracked is not at the target for motion compensation, a motion correlation model between the target and the device need to be established beforehand, and the tracked motion is then used together with the motion correlation model to derive the target motion.

Acknowledgements

[1] Cappato, et al., Worldwide Survey on the Methods, Efficacy, and Safety of Catheter Ablation for Human Atrial Fibrillation, Circulation 111 (2005) 1100–1105.

[2] Wazni, et al., Radiofrequency ablation vs antiarrhythmic drugs as first-line treatment of symptomatic atrial fibrillation: a randomized trial, JAMA 293 (21) (2005) 2634–2640.

[3] Zagorchev, et al., Rapid fusion of 2D x-ray fluoroscopy with 3D multi-slice CT for image-guided electrophysiology procedures, in: K. R. Cleary, M. I. Miga (Eds.), Proceedings of SPIE: Medical Imaging 2007: Visualization and Image-Guided Procedures, Vol. 6509, 2007, p. pp. 65092B.

[4] Sra, et al., Computed Tomography-Fluoroscopy Image Integration-Guided Catheter Ablation of Atrial Fibrillation, J Cardiovasc Electrophysiol 18 (4) (2007) 409–414.

[5] Ector, et al., Biplane three-dimensional augmented fluoroscopy as single navigation tool for ablation of atrial fibrillation: Accuracy and clinical value, Heart Rhythm 5 (7) (2008) 957–964.

[6] Knecht, et al., Computed tomography-fluoroscopy overlay evaluation during catheter ablation of left atrial arrhythmia, Europace 10 (2008) 931–938.

[7] P. H. Hertrich, Practical Radiography - Principles and Applications, 1st Edition, Publicis Corporate Publishing, Erlangen, 2005.

[8] A. Oppelt (Ed.), Imaging Systems for Medical Diagnostics, 2nd Edition, Publicis Corporate Publishing, Erlangen, 2005.

[9] Orlov, et al., Three-dimensional rotational angiography of the left atrium and esophagus: a virtual computed tomography scan in the electrophysiology lab?, Heart Rhythm 4 (1) (2007) 37–43.

[10] Al-Ahmad, et al., Time-resolved three-dimensional imaging of the left atrium and pulmonary veins in the interventional suite: A comparison between multisweep gated rotational three-dimensional reconstructed fluoroscopy and multislice computed tomography, Heart Rhythm 5 (4) (2008) 513–519.

[11] Nölker, et al., Three-dimensional left atrial and esophagus reconstruction using cardiac C-arm computed tomography with image integration into fluoroscopic views for ablation of atrial fibrillation: Accuracy of a novel modality in comparison with multislice computed tomography, Heart Rhythm 5 (12) (2008) 1651–1657.

[12] Strobel, et al., Imaging with Flat-Detector C-Arm Systems, in: M. F. Reiser, C. R. Becker, K. Nikolaou, G. Glazer (Eds.), Multislice CT (Medical Radiology / Diagnostic Imaging), 3rd Edition, Springer Berlin / Heidelberg, 2009, Ch. 3, pp. 33–51.

[13] Pruemmer, et al., Cardiac C-arm CT: a unified framework for motion estimation and dynamic CT, IEEE Trans Med Imaging 28 (11) (2009) 1836–1849.

[14] Lauritsch, et al., Towards cardiac C-arm computed tomography, IEEE Trans Med Imaging 28 (7) (2006) 922–34.

[15] Savard, et al., Fluoroscopic Navigation System to Guide Catheter Ablation in Cardiac Arrhythmias, First Experiences, Conf Proc IEEE Eng Med Biol Soc (2003) 238–142.

[16] Sun, et al., Registration of high-resolution 3D atrial images with electroanatomical cardiac mapping: evaluation of registration methodology, Vol. 5744, SPIE, 2005, pp. 299–307.

[17] Kistler, et al., The impact of image integration on catheter ablation of atrial fibrillation using electroanatomic mapping: a prospective randomized study, Eur Heart J 29 (24) (2008) 3029–3036.

[18] Bertaglia, et al., Image integration increases efficacy of paroxysmal atrial fibrillation catheter ablation: results from the CartoMergeTM Italian Registry, Europace 11 (8) (2009) 1004–1010.

[19] Timinger, et al., Motion Compensated Coronary Interventional Navigation by Means of Diaphram Tracking and Elastic Motion Models, Phys. Med. Biol. 50 (3) (2005) 491–503.

[20] Ross, et al., Motion Correction For Augmented Fluoroscopy - Application To Liver Embolization, in: Proc IEEE Int Symp Biomed Imaging, ISBI, 2008, pp. 1553–1556.

[21] Atasoy, et al., Real-time Respiratory Motion Tracking: Roadmap Correction for Hepatic Artery Catheterizations, in: Proceedings of SPIE Medical Imaging, Vol. 6918, San Diego, CA, USA, 2008, p. 691815.

[22] Borgerta, et al., Respiratory motion compensation with tracked internal and external sensors during CT guided procedures, International Congress Series 1281 (2005) 577–582.

[23] McLeish, et al., A study of the motion and deformation of the heart due to respiration, IEEE Trans Med Imaging 21 (9) (2002) 1142–1150.

[24] Shechter, et al., Displacement and velocity of the coronary arteries: cardiac and respiratory motion, IEEE Trans Med Imaging 25 (3) (2006) 369–375.

[25] Shechter et al., Prospective motion correction of x-ray images for coronary interventions, IEEE Trans Med Imaging 24 (4) (2005) 441–450.

[26] Shechter et al., Respiratory motion of the heart from free breathing coronary angiograms, IEEE Trans Med Imaging 23 (8) (2004) 1046–1056.

[27] King et al., A subject-specific technique for respiratory motion correction in image-guided cardiac catheterisation procedures, Med Image Anal 13 (3) (2009) 419–331.

[28] AAPM Task Group 76, The management of respiratory motion in radiation oncology, AAPM Report 91, American Association of Physicists in Medicine (July 2006).

[29] Brost et al., 3-D Respiratory Motion Compensation during EP Procedures by Image-Based 3-D Lasso Catheter Model Generation and Tracking, in: G.-Z. Yang, D. J. Hawkes, D. Rueckert, J. A. Noble, C. J. Taylor (Eds.), Lect. Notes Comput. Sci., Vol. 5761, London, 2009, pp. 394–401.

[30] Liao, et al., Location Constraint Based 2D-3D Registration of Fluoroscopic Images of CT Volumes for Image-Guided EP Procedures, in: Proceedings of SPIE Medical Imaging, Vol. 6918, 2008, pp. 69182T–1–69182T–8.

[31] Halir, and Flusser, Numerically Stable Direct Least Squares Fitting Of Ellipses, in: In Proceedings of the 6th Conference in Central Europe on Computer Graphics and Visualization, Plzen, 1998, pp. 253–257.

[32] Hartley and Zisserman, Multiple View Geometry in Computer Vision, 2nd Edition, Cambridge University Press, ISBN: 0521540518, Cambridge, New York, Melbourne, Madrid, Cape Town, Singapore, São Paulo, Delhi, 2004.

[33] Fitzgibbon, et al., Direct least square fitting of ellipses, IEEE Trans Pattern Anal Mach Intell 21 (5) (1999) 476–480.

[34] Fitzgibbon and Fisher, A Buyer's Guide to Conic Fitting, in: BMVC '95: Proceedings of the 6th British conference on Machine Vision, Vol. 2, BMVA Press, Surrey, UK, 1995, pp. 513–522.

[35] Brost, et al., Geometric Accuracy of 3-D X-Ray Image-Based Localization from Two C-Arm Views, in: L. Joskowicz, P. Abolmaesumi, M. Fitzpatrick (Eds.), Workshop on Geometric Accuracy In Image Guided Interventions - Medical Image Computing and Computer Assisted Interventions 2009, MICCAI, London UK, 2009, pp. 12–19.

[36] Brost, et al., Accuracy of x-ray image-based 3D localization from two C-arm views: a comparison between an ideal system and a real device, in: M. I. Miga, K. H. Wong (Eds.), Medical Imaging 2009: Visualization, Image-Guided Procedures, and Modeling, Vol. 7261, SPIE, Lake Buena Vista, FL, USA, 2009, p. 72611Z.

[37] L. Quan, Conic Reconstruction and Correspondence From Two Views, IEEE Trans Pattern Anal Mach Intell 18 (2) (1996) 151–160.

[38] Sato, et al., 3D Multi-Scale Line Filter for Segmentation and Visualization of Curvilinear Structures in Medical Images, Med Image Anal 2 (2) (1998) 143–168.

[39] N. Otsu, A Threshold Selection Method from Gray-Level Histograms, IEEE Trans Syst Man Cybern 9 (1) (1979) 62–66.

[40] Breu, et al., Linear time Euclidean distance transform algorithms, IEEE Trans Pattern Anal Mach Intell 17 (1995) 529–533.

[41] Duda et al., Pattern Classification, 2nd Edition, John Wiley & Sons, Inc, 2000.

[42] Bronstein, et al., Taschenbuch der Mathematik, Fifth Edition, Verlag Harri Deutsch, Frankfurt, 2001.

[43] Rougee, et al., Geometrical calibration for 3D x-ray imaging, in: Y. Kim (Ed.), Proceedings of SPIE Medical Imaging 1993: Image Capture, Formatting, and Display, Vol. 1897, SPIE, 1993, pp. 161–169.

[44] Ector, et al., Changes in Left Atrial Anatomy Due to Respiration: Impact on Three-Dimensional Image Integration During Atrial Fibrillation Ablation, J Cardiovasc Electrophysiol 19 (8).

[45] Baert, et al., Guide Wire Tracking During Endovascular Interventions, IEEE Trans Med Imaging 22 (8) (2003) 965–972.

[46] Elgort, et al., Real-Time Catheter Tracking and Adaptive Imaging, J Magn Reson Imaging 18 (5) (2003) 621–626.

[47] Esteghamatian, et al., Real-time 2D-3D MR cardiac image registration during respiration using extended Kalman filter predictors, in: 9th International Conference on Signal Processing (ICSP 2008), IEEE, Bejing, China, 2008, pp. 1325–1328.

[48] Manke et al., Model Evaluation and Calibration for Prospective Respiratory Motion Correction in Coronary MR Angiography Based on 3-D Image Registration, IEEE Transactions On Medical Imaging 21 (9) (2002) 1132 – 1141.